Available online at www.sciencedirect.com
ScienceDirect
Trans. Nonferrous Met. Soc. China 34(2024) 1804−1816
Transactions of Nonferrous Metals Society of China
www.tnmsc.cn

Microstructure and mechanical properties of Mg−Gd−Y−Zn−Zr alloy plates with different initial textures after hot rolling

Han CHEN, Zhang HU, Yu-xiang HAN, Tao CHEN, Chu-ming LIU, Zhi-yong CHEN

School of Materials Science and Engineering, Central South University, Changsha 410083, China

Received 18 December 2022; accepted 15 May 2023

Abstract: The effects of initial textures on the microstructures and mechanical properties of rolled Mg−4.7Gd−3.4Y−1.2Zn−0.5Zr (wt.%) plates were studied by optical microscope (OM), scanning electron microscope (SEM), electron backscatter diffraction (EBSD), transmission electron microscope (TEM) and tensile test. In the plate with an initial texture of ⟨0001⟩//RD (rolling direction), relatively coarse grains and bimodal basal texture are developed. However, in the plate with an initial texture of ⟨0001⟩//TD (transverse direction), finer grain size and strong ⟨0001⟩//ND basal textures are obtained due to the higher degree of dynamic recrystallization during rolling. Additionally, the irregular-shaped long-period stacking ordered (LPSO) phases are elongated along RD in both plates, which results in anisotropic load-bearing strengthening behavior, and further leads to a certain degree of yield anisotropy. The analysis of the strengthening mechanism shows that grain boundary strengthening is the most effective strengthening method in the plates. Because of the finer grain size and the strengthening caused by the elongated irregular-shaped LPSO phases, the rolled plate with an initial ⟨0001⟩//TD texture achieves the highest yield strength along RD.

Key words: Mg−Gd−Y−Zn−Zr alloy; texture; LPSO phase; mechanical properties; strengthening mechanism

1 Introduction

As the lightweight structural materials, magnesium (Mg) alloys have great application potential in the fields of computer, communication, consumer electronic (3C), aerospace, automotive, and other industries [1−4]. Among many Mg alloys, Mg−RE (rare earth elements)−Zn alloys containing long-period stacking ordered (LPSO) phase have been widely studied [5−7]. In 2001, KAWAMURA et al [8] prepared $Mg_{97}Zn_1Y_2$ alloy with a tensile strength of ~600 MPa and elongation of ~5% by rapidly solidified powder metallurgy, and they attributed the remarkable properties to the existence of nanocrystalline and LPSO phase in this alloy. XU et al [9] fabricated an Mg−8.2Gd−3.8Y−1.0Zn−0.4Zr (wt.%) alloy with a tensile strength of 505 MPa and a yield strength of 416 MPa by vertical direct chill casting, extrusion, hot rolling and peak-aging treatment. The significant increase in strength is related to the fine β' phase, grains with strong basal texture, and the dispersed LPSO phases. In brief, it is critical to further improve the mechanical properties of Mg−RE−Zn alloy by tailoring the microstructure through appropriate deformation.

The deformation modes activated during the deformation significantly affect the microstructure of Mg alloy. Generally speaking, basal $\langle a\rangle$ slip and $\{10\bar{1}2\}$ twinning are the most common deformation modes, but for Mg alloys containing the LPSO phase, they are inhibited to some extent [10]. As reported by MATSUDA et al [11], the critical resolved shear stress (CRSS) of basal $\langle a\rangle$ slip could be increased by the presence of the

Corresponding author: Zhi-yong CHEN, Tel: +86-13974926019, E-mail: czysh@netease.com
DOI: 10.1016/S1003-6326(24)66508-8

intragranular lamellar LPSO phase. SHAO et al [12] observed that the LPSO phase with a thickness exceeding 12 nm could not be twinned. It must be pointed out that the activations of basal $\langle a\rangle$ slip and $\{10\bar{1}2\}$ twinning are insufficient to meet the requirement of Taylor's criterion for continuous deformation [13]. Therefore, non-basal slip, such as prismatic $\langle a\rangle$ slip, is also an essential deformation mode of Mg alloy [14−16]. Besides, as an unusual deformation mode, kinking is also frequently observed in Mg−RE−Zn alloys containing the LPSO phases. According to the report of HAGIHARA et al [17], in order to accommodate the strain of *c*-axis, kinking is more likely to occur when the basal $\langle a\rangle$ slip and $\{10\bar{1}2\}$ twinning are restrained.

The crystal orientation plays a decisive role in selecting the deformation mode during the deformation [18−20]. Furthermore, significant differences in the microstructure, particularly deformation texture, could be caused by varying the lattice rotations resulting from different deformation modes. As pointed out by YI et al [21], when the *c*-axis of grain lies nearly perpendicular to the loading direction, high stress is needed for the activation of basal $\langle a\rangle$ slip. Under the high-stress state, non-basal $\langle a\rangle$ slip is also activated, and then the activity of basal $\langle a\rangle$ slip decreases rapidly. On the contrary, when the *c*-axis of grain is parallel to the loading direction, $\{10\bar{1}2\}$ twinning plays an important role in deformation, and the activation of $\{10\bar{1}2\}$ twinning leads to rapid changes in texture. To study the deformation mechanism and related texture evolution of AZ31 Mg alloys, HU et al [22] carried out uniaxial tension and visco-plastic self-consistent (VPSC) analysis on extruded AZ31 alloy with a rare non-basal texture. It is found that when $\{10\bar{1}2\}$ twinning serves as a carrier of deformation, it mainly results in the formation of basal texture. However, the role of $\{10\bar{1}2\}$ twinning is just to accommodate local strain, which mainly brings about the formation of prismatic texture.

In summary, the initial texture will affect the deformation modes, the microstructures, and the mechanical properties. There are few studies on the microstructure and texture of the rolled plates with different initial textures, especially Mg−Gd−Y−Zn−Zr plates containing the LPSO phase. Therefore, in this work, two Mg−4.7Gd−3.4Y−1.2Zn−0.5Zr (wt.%) plates containing LPSO phase with different initial textures were prepared and then subjected to hot rolling. The microstructures and textures of rolled plates are compared. The correlation between microstructures and mechanical properties is systematically investigated.

2 Experimental

2.1 Hot rolling

An extruded Mg−4.7Gd−3.4Y−1.2Zn−0.5Zr (wt.%) alloy plate with a texture of $\langle 0001\rangle$//ED (extrusion direction) was used as the starting material in this work. For preparing plates with different initial textures, two plates with a dimension of 120 mm × 60 mm × 14 mm were cut from the center of the extruded plate along the TD (transverse direction, Sample T) and ED (Sample E), respectively. The plates were preheated to 450 °C for 1 h, and then rolled to a total reduction of 68% by multi-pass hot rolling with a speed of 0.36 m/s. Before each pass, the plates were returned to the resistance furnace for 10 min to keep the rolling temperature at 450 °C. After the final pass, water quenching was performed on the plates immediately. The directions of the rolled plate were abbreviated as RD (rolling direction), TD (transverse direction), and ND (normal direction).

2.2 Microstructure characterization and mechanical property tests

Specimens for optical microscopy (OM) observation were ground, polished, and finally chemically etched in a solution of 2.1 g picric acid, 35 mL ethanol, 5 mL acetic acid, and 35 mL water. Phase morphology detection was carried out on FEI Sirion200 scanning electron microscopy (SEM). Bright-field images and corresponding selected area electron diffraction (SAED) patterns were obtained using an FEI Tecnai G2 F20 transmission electron microscopy (TEM). Crystal orientation was analyzed using an electron backscatter diffraction (EBSD) detector (Helios Nanolab 600i) and AztecCrystal software. All the TEM and EBSD specimens were polished by twin-jet electrolysis with a solution of 260 mL ethanol and 10 mL perchloric acid at −30 °C. The values of irregular-shaped LPSO phases were measured using Photoshop and Image-Pro Plus 6.0 from low-magnification SEM images. For the tensile tests, dog-bone-shaped specimens with gauge dimensions of 15 mm × 6 mm × 2 mm were cut along the RD (hereafter denoted as RD specimen) and TD (hereafter denoted as TD specimen) of the rolled plates, respectively. The mechanical properties were evaluated by conducting tensile tests on an Instron 3369 tester at a speed of 1 mm/min at ambient temperature, and the strain rate of the tensile test is $1\times10^{-3}\ s^{-1}$. The tensile yield strength (σ_{TYS}), ultimate tensile strength (σ_{UTS}), and elongation to failure (ε_f) were obtained based on the average value of three tests. The experimental processes are illustrated in Fig. 1.

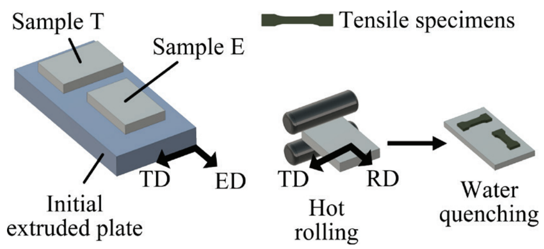

Fig. 1 Experimental processes and sampling methods of tensile specimens

3 Results

3.1 Initial microstructure

The microstructure and texture of the initial extruded plate are shown in Fig. 2. Many second phases with different morphologies can be observed. Our previous study confirmed that the lamellar intragranular phases (marked by red triangles) and the irregular-shaped intergranular phases (marked by yellow triangles) in this extruded plate are 14H-LPSO phases [23]. Since there is no LPSO phase standard pattern in the EBSD database, the diffraction pattern of LPSO phase cannot be analyzed. Thus, the EBSD results in this study only represent the crystal orientation of the α-Mg matrix. The pole figures in Fig. 2(c) indicate that this extruded plate has a strong texture of ⟨0001⟩//ED, which is an unusual extruded texture of Mg alloy. Some researchers attribute the formation of this unusual texture to the preferential growth of recrystallized grains [24−27].

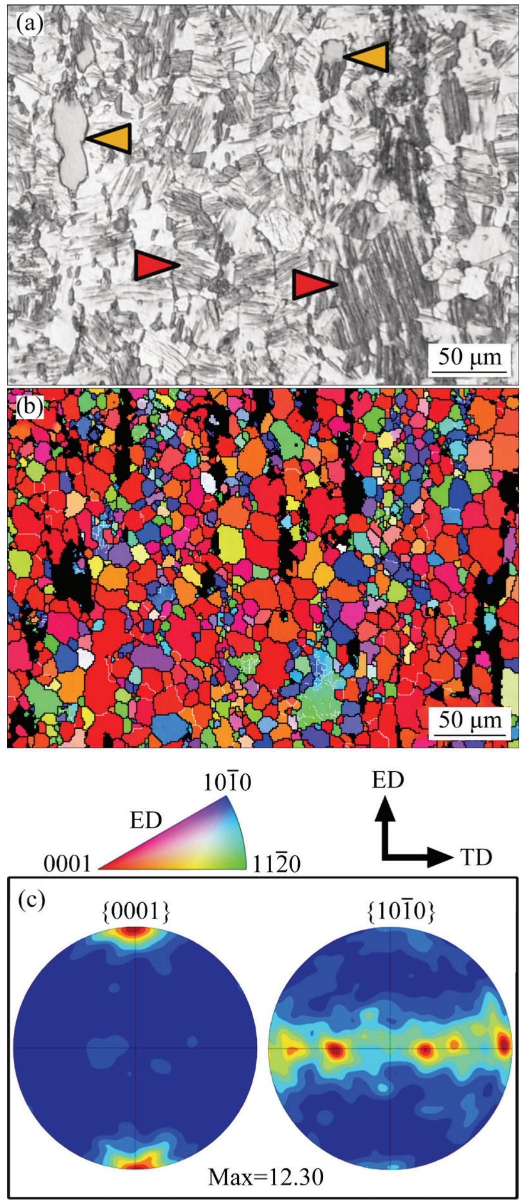

Fig. 2 Microstructures and texture of initial extruded plate: (a) OM image; (b) EBSD map; (c) Pole figures

The plates before rolling are cut along the TD and ED of the extruded plate, respectively (as shown in Fig. 1). Naturally, from the coordinate system of rolled plates, the initial textures of the two plates are ⟨0001⟩//TD (Sample T) and ⟨0001⟩//RD (Sample E), as shown in Figs. 3(a) and (b), and they are exactly different initial textures.

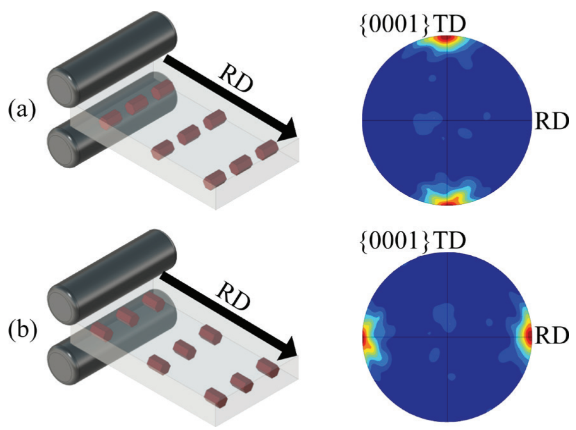

Fig. 3 Initial textures of rolled plates: (a) Sample T; (b) Sample E

3.2 Microstructure after rolling

Figure 4 shows the OM images observed from the center of the ND−RD plane. After rolling, irregular-shaped LPSO phases (marked by blue triangles) and rod-shaped LPSO phases (marked by green triangles) are found in the rolled plates. The irregular-shaped LPSO phases are elongated along the RD, and the rod-shaped LPSO phases were broken from the irregular-shaped LPSO phase due to the severe deformation and dynamic recrystallization (DRX) during hot deformation [23]. However, the sizes of the rod-shaped LPSO phases are small, and it is likely to have negligible effects on the microstructures and mechanical properties of the alloy. What's more, a few lamellar LPSO phases (marked by red dotted lines) are observed in Sample T except for the irregular-shaped LPSO phases and rod-shaped LPSO phases, as shown in Figs. 4(a) and (b).

To better observe the morphology of the LPSO phase, the SEM-BSE (backscatter electron mode of SEM) detection was operated. Figure 5 shows the SEM-BSE images observed from the center of the ND−RD plane. Consistent with the OM images in Fig. 4, the irregular-shaped LPSO phases (marked by blue triangles) elongated along the RD, and the rod-shaped LPSO phases (marked by green triangles) are found. Through careful observation, some bending lamellar LPSO phases are also characterized in Sample T (marked by red dotted lines).

To further identify the stacking structure of the LPSO phase, TEM observation was performed on the rolled plates. Since the bright-filed images and SAED patterns recorded from the areas containing LPSO phase are quite similar, there is only one set of images provided in Fig. 6. With the electron beam (EB) parallel to $[11\bar{2}0]_\alpha$, many streaks parallel to $(0001)_\alpha$ appear in the bright field image, presenting typical characteristics of the LPSO phase. The corresponding SAED pattern of the LPSO phase shows 13 equal spacing diffraction spots between the $(0000)_\alpha$ and $(0002)_\alpha$ diffraction spots, which means that the LPSO phase has a 14H stacking structure.

Figure 7 shows the EBSD results observed from the center of the ND−RD plane, and the grains in the EBSD map are colored relative to the ND. Owing to the *c*-axis of the red grain being parallel to the ND, many red grains in the EBSD map preliminarily suggest that a strong texture is formed in the rolled plates. The high-angle grain boundaries (HAGBs), with misorientation angles higher than 15°, are highlighted by black solid lines.

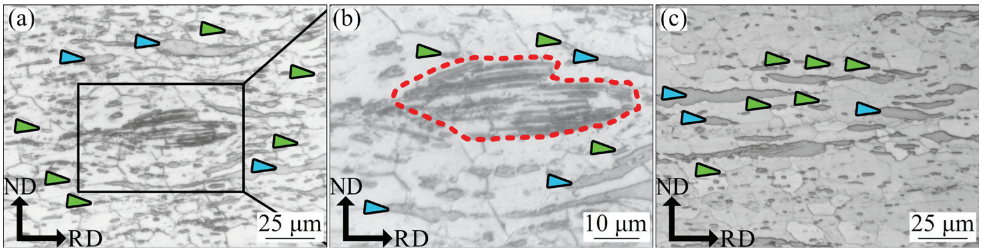

Fig. 4 OM images observed from ND−RD plane: (a, b) Sample T; (c) Sample E

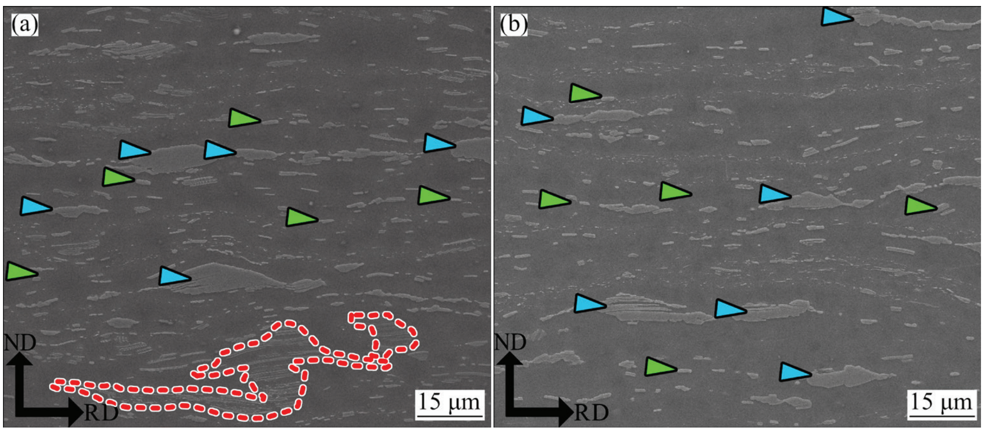

Fig. 5 SEM-BSE images of rolled plates: (a) Sample T; (b) Sample E

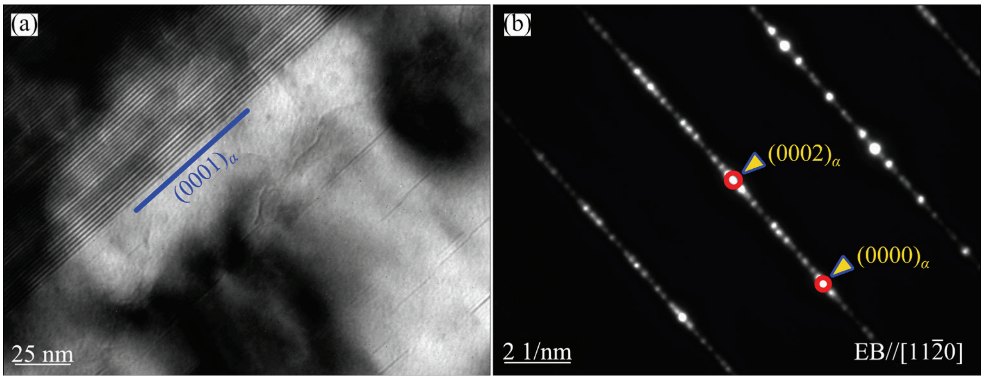

Fig. 6 TEM results of rolled plates: (a) Bright-field image; (b) SAED pattern

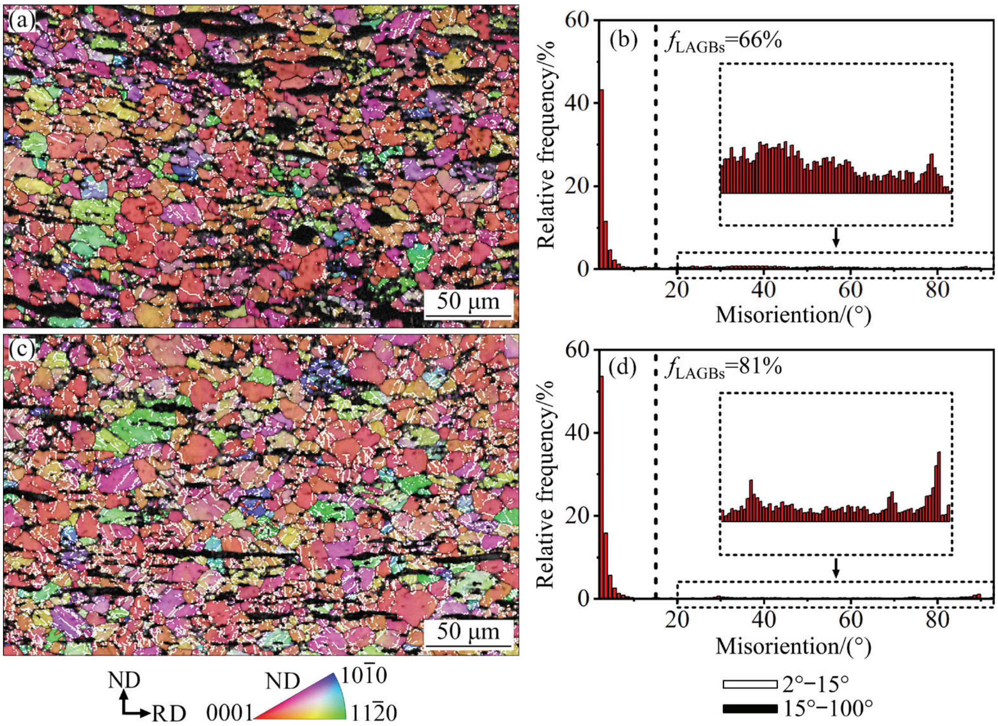

Fig. 7 EBSD maps (a, c) and grain boundary misorientation (b, d) of rolled plates: (a, b) Sample T; (c, d) Sample E

The low-angle grain boundaries (LAGBs), with misorientation angles higher than 2° and lower than 15°, are highlighted by white solid lines. The rolled microstructures of the two plates are composed of abundant LAGBs, indicating a high degree of rolling deformation. Further statistics shows that the proportion of LAGBs in Sample T is 66%, while the proportion of LAGBs in Sample E is 81%, and the proportion of LAGBs in Sample T is fewer than that in Sample E.

Grain orientation spread (GOS) can be used to distinguish recrystallized grains. In this work, grains with GOS less than 2° (represented by blue) are considered dynamic recrystallized (DRXed) grains [27,28]. As shown in Figs. 8(a) and (c), the number of DRXed grains in Sample T is higher than that in Sample E, and the volume fraction of DRXed grains is 23.6% in Sample T while 8.4% in Sample E. Combined with the results of EBSD, it can be deduced that Sample T has experienced more severe DRX than Sample E, resulting in finer grains. As shown in Figs. 8(b) and (d), the average grain size of Sample T is 8.1 μm, which is finer than that of Sample E (12.5 μm).

The {0001} and {10$\bar{1}$0} pole figures of the two rolled plates shown in Fig. 9 determine that both rolled plates exhibit a basal texture. But there are still some differences between them. For Sample T, as shown in Fig. 9(a), the maximum intensity of the {0001} pole figure is 8.3, and the

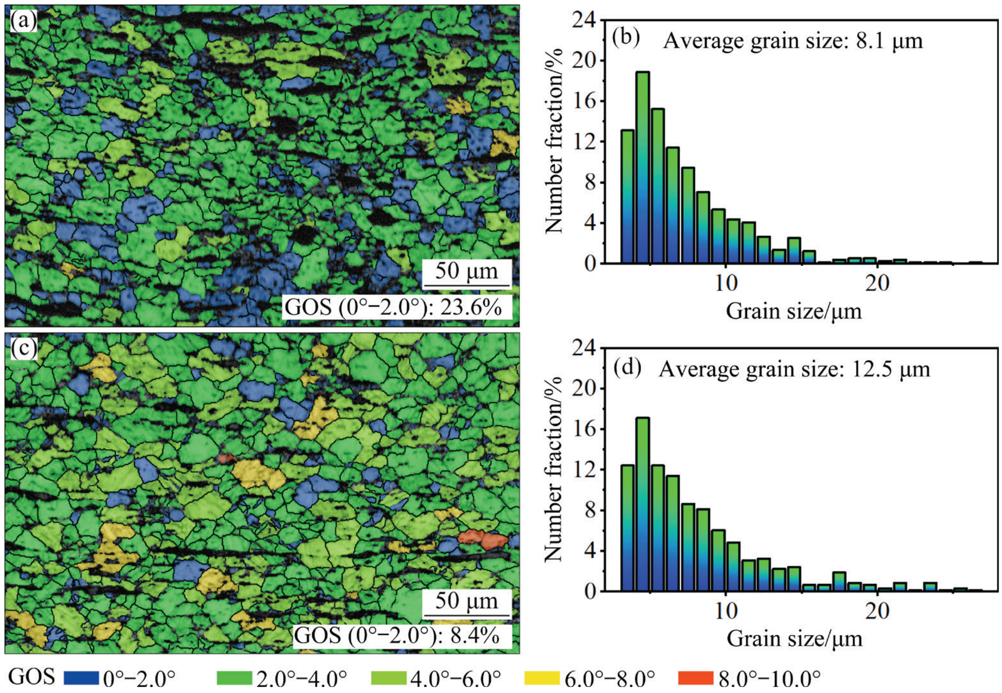

Fig. 8 GOS distribution maps (a, c) and grain size (b, d) of rolled plates: (a, b) Sample T; (c, d) Sample E

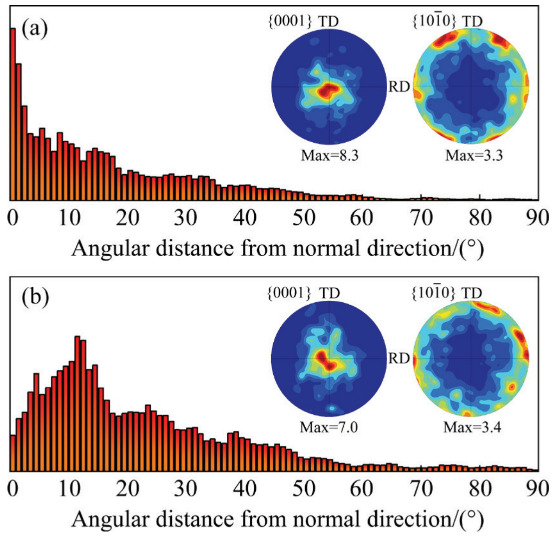

Fig. 9 {0001} and {10$\bar{1}$0} pole figures and distribution statistics of angular distance from ND in {0001} pole figures: (a) Sample T; (b) Sample E

basal pole is concentrated in the ND. For Sample E, as shown in Fig. 9(b), the maximum intensity of the {0001} pole figure is 7.0, and the basal pole is concentrated in two regions away from the ND, forming a bimodal basal texture. The angular distance from the ND in {0001} pole figures of the two rolled plates was displayed, only the angle of basal pole deviation from ND is calculated, and it is not known in which direction the basal pole is deflected. Nevertheless, combined with the {0001} pole figures, it still can be found from the statistics that Sample E obtains a bimodal basal texture of the basal pole deviating from the ND of 10°−15°, while in Sample T a strong basal texture of ⟨0001⟩//ND is formed.

3.3 Mechanical properties

The engineering stress−strain curves obtained along the RD and TD of the rolled plates are shown in Fig. 10(a). Within the same plate, the curves of two different tensile specimens show an apparent difference. The $\sigma_{\rm TYS}$ and $\sigma_{\rm UTS}$ along the RD are always higher than those along the TD. Within the same direction, the $\sigma_{\rm TYS}$ and $\sigma_{\rm UTS}$ of Sample T are always higher than those of Sample E. A summary of the mechanical properties shown in Fig. 10(b) further highlights the distinction in the engineering stress−strain curves, and the in-plane yield anisotropy (YA, $A_{\rm Y}$) within the one plate is described as follows [29]:

$$A_{\rm Y}=\frac{\sigma_{\rm TYS}^{\max}-\sigma_{\rm TYS}^{\min}}{\sigma_{\rm TYS}^{\min}}\times 100\% \tag{1}$$

For Sample T, $\sigma_{\rm TYS}$ along the RD is 16 MPa higher than that along the TD, and the YA is 6.5%. For Sample E, $\sigma_{\rm TYS}$ along the RD is 12 MPa higher than that along the TD, and the YA is 5.3%. Both two rolled plates have a certain degree of yield anisotropy. Besides, within the same loading direction, σ_{TYS} along the TD of Sample T is 23 MPa higher than that of Sample E, and the σ_{TYS} along the RD of Sample T is 27 MPa higher than that of Sample E. All the rolled specimens have good ductility, and their ε_f ranges from 18% to 21%.

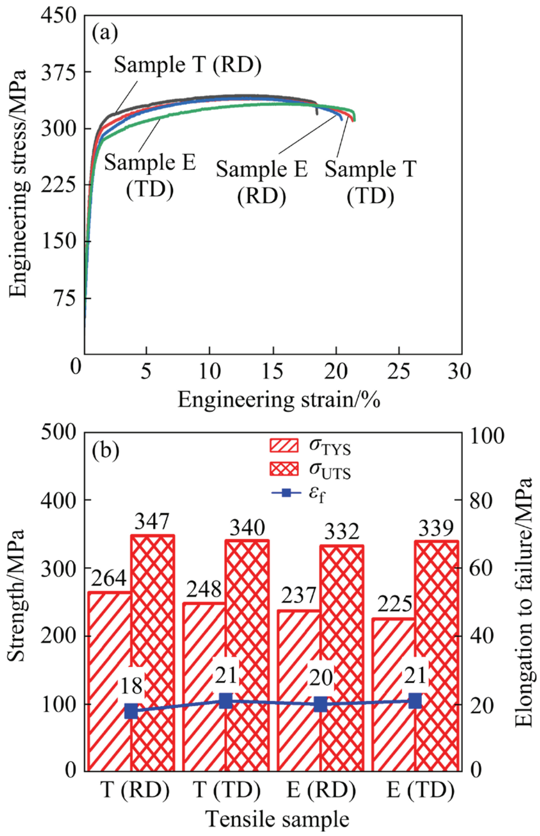

Fig. 10 Engineering stress−strain curves (a) and mechanical property statistics (b) of rolled specimens

Figure 11 shows the typical fracture morphologies of different tensile specimens. There is no apparent difference between the two tensile specimens. Many dimples with different sizes and a few cleavage surfaces can be found, these cleavage surfaces are very rough, and many fine streaks are distributed on them. The fracture morphologies indicate that the rolled plates have good ductility, consistent with the results of mechanical properties tests.

4 Discussion

4.1 Effect of initial texture on rolled microstructure

To explain the underlying effect of initial texture on rolled microstructure, the Schmid factors of basal $\langle a\rangle$ slip, prismatic $\langle a\rangle$ slip, and $\{10\bar{1}2\}$ twinning under rolling stress were calculated and projected on the {0001} pole figures, as shown in Fig. 12, where the red dashed ellipses represent the initial texture of Sample T in the {0001} pole figure, and the black dashed ellipses represent the initial texture of Sample E in the {0001} pole figure. By matching the {0001} pole figure of Sample T and the Schmid factor projection figures, it can be quickly figured out that the Schmid factors of basal $\langle a\rangle$ slip and $\{10\bar{1}2\}$ twinning of Sample T are low, and the Schmid factor of prismatic $\langle a\rangle$ slip is high. Therefore, basal $\langle a\rangle$ slip and $\{10\bar{1}2\}$ twinning are restrained, and the prismatic $\langle a\rangle$ slip is easy to activate at the early rolling stage. Moreover, for Sample E, it can be found that the Schmid factors of basal $\langle a\rangle$ slip and prismatic $\langle a\rangle$ slip are low, the Schmid factor of $\{10\bar{1}2\}$ twinning is high, and thus $\{10\bar{1}2\}$ twinning will be widely activated at the early rolling stage.

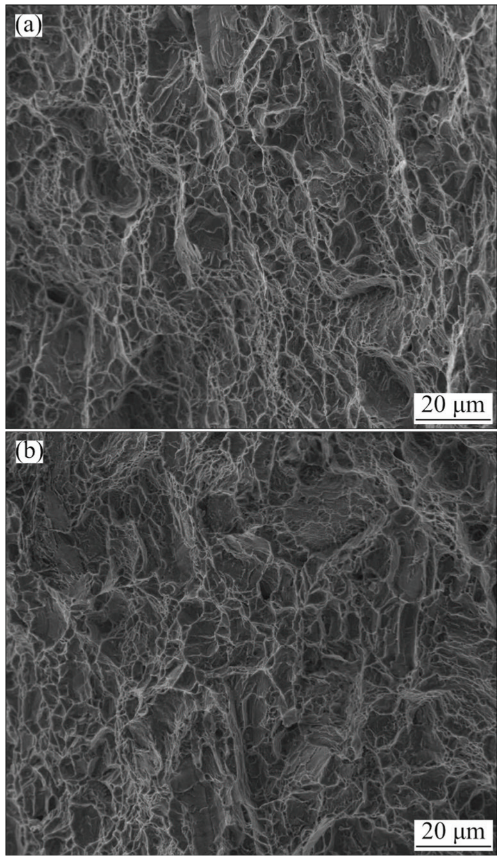

Fig. 11 Typical fracture morphologies of rolled plate: (a) Tension along RD; (b) Tension along TD

SHAO et al [30] have studied the rolling process of Mg−Gd−Y−Zn alloy containing LPSO phase, in which the kinking and $\{10\bar{1}2\}$ twinning in the early rolling stage have been investigated in

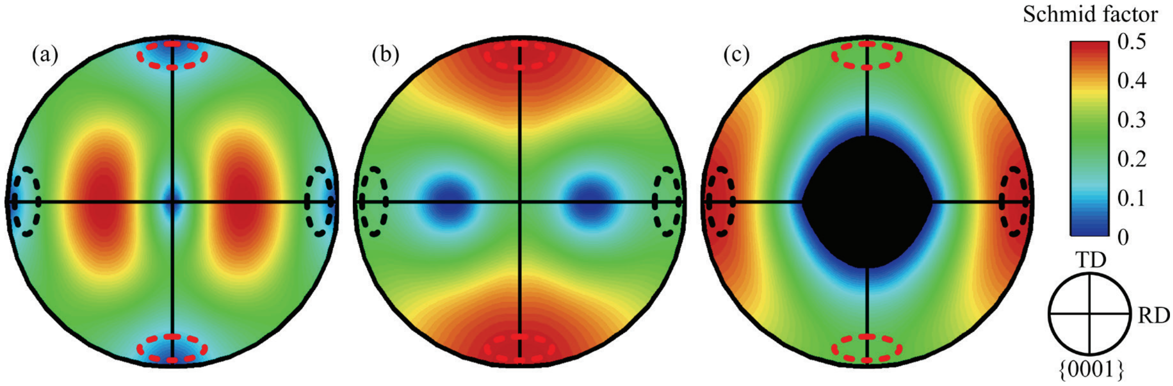

Fig. 12 Schmid factor projected on {0001} pole figures of selected deformation modes under rolling stress: (a) Basal ⟨*a*⟩ slip; (b) Prismatic ⟨*a*⟩ slip; (c) $\{10\bar{1}2\}$ twining

detail. Theoretically, in the Mg−RE−Zn alloys containing LPSO phase, kinking will be activated when the basal ⟨*a*⟩ slip and $\{10\bar{1}2\}$ twinning are restrained because prismatic ⟨*a*⟩ slip cannot accommodate the strain of the *c*-axis [30,31]. Accordingly, kinking is activated in Sample T to accommodate the *c*-axis strain during the early rolling stage. The kink boundaries are formed by dislocation accumulation [32], and as the strain increases, massive dislocations pile up at the kink boundaries, and then LAGBs are formed via dislocation climbing and rearrangement. As the deformation proceeds further, more dislocations are absorbed by LAGBs, and the misorientation of the *α*-Mg matrix on both sides of the kink boundaries is raised. When the dislocation accumulates to a certain extent, HAGBs and DRXed grains are formed through the continuous dynamic recrystallization (CDRX) mechanism. Therefore, the finer grains in Sample T are presumably ascribed to the more severe DRX promoted by kinking. In fact, kinking is already activated in the early rolling stage, and the kinked bands are eliminated efficiently by the DRX process, so that just a few lamellar LPSO phases with the characteristic of kinking can be observed in the SEM image of Sample T, as shown in Fig. 5(a).

For Sample E, almost no lamellar LPSO phases and twins can be observed, which may be related to the interaction between $\{10\bar{1}2\}$ twins and lamellar LPSO phases. At the early rolling stage, the $\{10\bar{1}2\}$ twining is well activated and the semi-coherent BP interface (basal−prismatic interface, the interface of lamellar LPSO phases' basal plane and the twins' prismatic plane) is formed. The sliding of periodic misfit dislocations at the BP interface during intermediate annealing of multi-pass hot rolled plates leads to the decomposition of the lamellar LPSO phases. The decomposition of the lamellar LPSO phases is beneficial to the relaxation of back stress and makes twins grow into new grains easily [33,34]. Moreover, at the later rolling stage, the bimodal basal texture of Sample E is not conducive to the activation of $\{10\bar{1}2\}$ twinning. It is worth noting that this experiment recorded the EBSD data of the last rolling pass, that is, the later rolling stage. Therefore, the lamellar LPSO phases and twins are difficult to be observed in Sample E.

The different volume fractions of DRXed and unDRXed grains further affect the textures of rolled plates. The inverse pole figures of the whole region, DRXed grains, and unDRXed grains are shown in Fig. 13. No matter in Sample T or in Sample E, a strong ⟨0001⟩//ND texture in the DRXed grains is formed, and the texture intensity of the DRXed grains is the highest. It should be pointed out that the recrystallization process can be divided into grain nucleation and grain growth. For some Mg alloys containing Gd and Y, although their grain nucleation is randomly oriented, there is a preferential phenomenon in grain growth, and grains with specific orientations are easier to grow and a recrystallization texture could be formed. The Mg−4.7Gd−3.4Y−1.2Zn−0.5Zr (wt.%) alloy used in this experiment does have the preferential growth of DRXed grains during the hot deformation. For example, an unusual ⟨0001⟩//ED texture is formed in the initial extruded plate, which differs from the texture of commonly extruded Mg alloy.

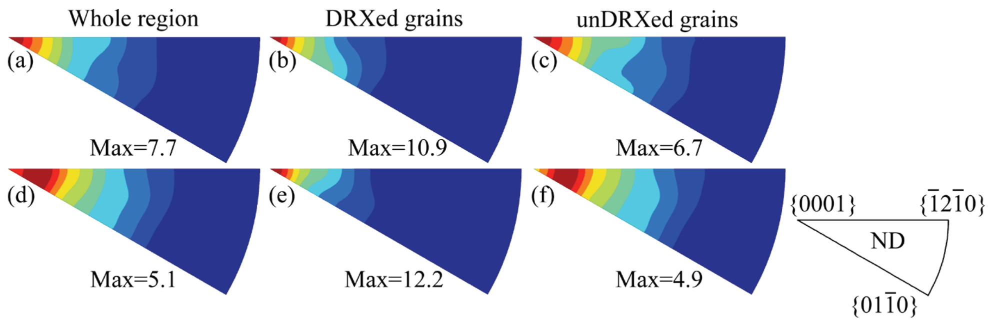

Fig. 13 Inverse pole figures of whole region, DRXed grains, and unDRXed grains: (a, b, c) Sample T; (d, e, f) Sample E

The recrystallization texture caused by the preferred growth of DRXed grains has been reported widely. The researchers pointed out that it may be related to the preferred growth caused by the drag effect of Gd/Y atoms during recrystallization [24−27]. In addition, this unusual texture may be also related to the lattice rotation caused by the activation of non-basal slip under high-temperature deformation [35]. Consequently, it is reasonable to speculate that the preferential growth of DRXed grains may still occur during the hot rolling. In this work, some DRXed grains recorded in the EBSD data may undergo the grain growth. Therefore, the intensity of the basal texture of the DRXed grains could be higher than that of the unDRXed grains. Based on the above analysis, it is deduced that the DRXed grains are intimately related to the basal texture of ⟨0001⟩//ND, while the unDRXed grains tend to weaken and scatter the basal texture. Due to the increased volume fraction of unDRXed grains in Sample E, a bimodal basal texture of the basal pole deviating from the ND is developed.

4.2 Effects of different strengthening mechanisms on mechanical properties

Based on the materials strengthening theory, the σ_{TYS} of rolled plates can be expressed as follows:

$$\sigma_{TYS}=\sigma_{gb}+\sigma_{ss}+\sigma_{lpso}+\sigma_{dis} \tag{2}$$

where σ_{gb} means the grain boundary strengthening, σ_{ss} means the solid-solution strengthening, σ_{lpso} means the load-bearing strengthening contributed by directionally arranged irregular-shaped LPSO phase, and σ_{dis} means the dislocation strengthening.

For the σ_{gb}, KWAK and KIM [36] deduced the modified Hall−Petch relationship of Mg alloy rolled plates with strong texture:

$$\sigma_{gb}=\sigma_0+k_{PH}d^{-1/2}=\frac{26.6}{F_S}+\frac{41.7}{F_S}d^{-1/2} \tag{3}$$

where σ_0 is the intrinsic strength of single crystal that represents the resistance of the lattice to dislocation motion, k_{PH} is the strengthening coefficient (H−P slope), F_S means the average Schmid factor of basal ⟨a⟩ slip, which is shown in Fig. 14, d means the average grain size of the two rolled plates (8.1 and 12.5 μm respectively, as shown in Fig. 8). Consequently, For Sample T, the calculated σ_{gb} is 159 MPa along RD and 165 MPa along TD. For Sample E, the calculated σ_{gb} is 154 MPa along RD and 150 MPa along TD. From Eq. (3), the lower the d and the F_S, the higher the σ_{gb}. The F_S is closely related to the crystal orientation and load direction. In other words, when loading in a specific direction, the F_S is closely related to the type and intensity of texture. However, as shown in Fig. 14, although the texture intensity of Sample T is higher than that of Sample E, the F_S is the same along the RD, which is 0.26. In a word, when tension along RD, the σ_{gb} of Sample T and Sample E is only affected by the average grain size, but not the texture.

The σ_{ss} can be calculated by the following equation [37]:

$$\sigma_{ss}=\left(K_{Gd}^{1/n}C_{Gd}+K_{Y}^{1/n}C_{Y}\right)^n \tag{4}$$

where K and C are the strengthening constant and the concentration of Gd and Y, respectively. Generally, n is equal to 2/3. Since the strengthening constants, K_{Gd} and K_Y, are very close (1168 MPa·at.%$^{-2/3}$ for Gd and 1249 MPa·at.%$^{-2/3}$ for Y), the σ_{ss} can be inferred to be proportional to $C^{2/3}$, and C can be simplified as the atomic fraction of Gd+Y [37]. The atomic fractions of Gd, Y, and Zn in this experiment are 0.8%, 1.0%, and

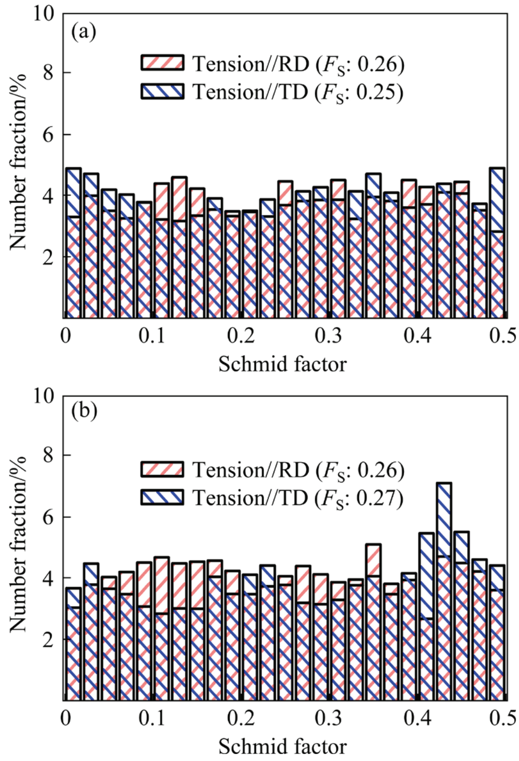

Fig. 14 Schmid factors of basal ⟨a⟩ slip of two rolled plates: (a) Sample T; (b) Sample E

0.5%, respectively. Due to the atomic ratio of Zn to RE in the LPSO phase being 1:1, by assuming that all Zn atoms participate in the formation of LPSO phase, the atomic fraction of Gd+Y participating in solid-solution strengthening is 1.3%. According to Ref. [38], when the atomic fraction of Gd+Y is 0.6%, the σ_{ss} is 38 MPa. Therefore, the calculated σ_{ss} in the current two rolled plates are 64 MPa.

The load-bearing strengthening induced by the elongated irregular-shaped LPSO phase (σ_{lpso}) is given as follows [39]:

$$\sigma_{lpso}=\frac{sV_P}{2}\sigma_m \tag{5}$$

where s is the aspect ratio of the average length to average diameter of the elongated irregular-shaped LPSO phases, V_P is the volume fraction of elongated irregular-shaped LPSO phases, and σ_m is the strength of the α-Mg matrix (210 MPa). The V_P, s and the calculated σ_{lpso} are listed in Table 1. The s values of all TD specimens are too small to affect the load-bearing strengthening (for example, the s of T specimen along TD is 1/8.82 and calculated σ_{lpso} is only 0.27 MPa), and thus the calculated σ_{lpso} of all TD specimens is negligible.

The σ_{dis} is related to the average density of geometry necessary dislocation (ρ_{GND}). The ρ_{GND} varies significantly by using different calculated methods, so the ρ_{GND} and σ_{dis} are not calculated in this experiment. However, what no one doubts is that the contribution of σ_{dis} to the σ_{TYS} exists. According to previous studies [40−42], the ρ_{GND} of wrought Mg ranges from 10^{13} to 10^{15} m^{-2}, and the σ_{dis} is dozens of MPa. Therefore, it is believed that the σ_{dis} in the rolled plates are the average σ_{TYS} of two tensile directions minus σ_{gb}, σ_{ss} and σ_{lpso}, which is 21 MPa in Sample T and 16 MPa in Sample E, respectively.

Figure 15 shows the calculated σ_{gb}, σ_{ss}, σ_{lpso}, σ_{dis} and σ_{TYS} of all the tensile specimens. In brief, the difference in yield strength between the two rolled plates can be well explained by grain boundary, dislocation, solid-solution, and LPSO phase load-bearing strengthening mechanisms. Grain boundary strengthening is the most effective strengthening method for the current rolled plates. According to the calculation, the σ_{gb}, σ_{ss} and σ_{dis} within the same rolled plate along two directions are almost the same. Thus, the yield anisotropy

Table 1 V_P, s and calculated σ_{lpso} of all tensile specimens

Specimen	V_P/%	s	σ_{lpso}/MPa	$\Delta\sigma_{lpso}$/MPa
T (RD)	2.03	8.82	19	19
T (TD)	2.03	0.11	−	
E (RD)	1.70	7.33	13	13
E (TD)	1.70	0.14	−	

The defined length of elongated irregular-shaped LPSO phase is parallel to RD; irregular-shaped LPSO phases are selected and highlighted in low-magnification SEM images, and then V_P and s of highlighted area are calculated

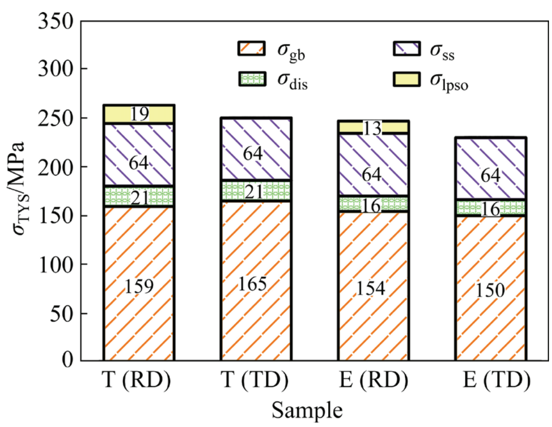

Fig. 15 Calculated σ_{gb}, σ_{ss}, σ_{lpso}, σ_{dis} and σ_{TYS} of rolled samples

must derive from other aspects. The irregular-shaped LPSO phase in the rolled plates is elongated, and the calculated $\Delta\sigma_{lpso}$ is numerically close to the difference in yield strength along two directions within a rolled plate. Therefore, it can be concluded that the anisotropic load-bearing strengthening behavior induced by the elongated irregular-shaped LPSO phase plays a critical role in yield anisotropy.

5 Conclusions

(1) After rolling, the plate with an initial texture of ⟨0001⟩//RD obtains relatively coarse grains and a bimodal basal texture of basal pole deviating from the ND of 10°−15°. However, due to the higher degree of dynamic recrystallization during rolling, the plate with an initial texture of ⟨0001⟩//TD obtains finer grains and a strong basal texture of ⟨0001⟩//ND.

(2) The irregular-shaped LPSO phases are elongated along RD in both plates, which results in anisotropic strengthening behavior, and further leads to a certain degree of yield anisotropy.

(3) Grain boundary strengthening is the most effective strengthening method in the plates. Because of the relatively finer grain size and the load-bearing strengthening caused by the elongated irregular-shaped LPSO phases, the rolled plate with an initial ⟨0001⟩//TD texture achieves the highest yield strength along RD.

CRediT authorship contribution statement

Han CHEN: Investigation, Data curation, Writing − Original draft; **Zhang HU:** Investigation, Data curation; **Yu-xiang HAN:** Writing − Review & editing; **Tao CHEN:** Writing − Review & editing; **Chu-ming LIU:** Validation, Resources; **Zhi-yong CHEN:** Supervision.

Declaration of competing interest

The authors declare that they have no known competing financial interests or personal relationships that could have appeared to influence the work reported in this paper.

Acknowledgments

The authors acknowledge the financial support from the National Natural Science Foundation of China (No. 51874367).

References

[1] SONG Jiang-feng, SHE Jia, CHEN Dao-lun, PAN Fu-sheng. Latest research advances on magnesium and magnesium alloys worldwide [J]. Journal of Magnesium and Alloys, 2020, 8: 1−41.

[2] WU Guo-hua, WANG Cun-long, SUN Ming, DING Wen-jiang. Recent developments and applications on high-performance cast magnesium rare-earth alloys [J]. Journal of Magnesium and Alloys, 2021, 9: 1−20.

[3] DING Zhi-bing, ZHAO Yu-hong, LU Ruo-peng, YUAN Mei-ni, WANG Zhi-jun, LI Hui-jun, HOU Hua. Effect of Zn addition on microstructure and mechanical properties of cast Mg−Gd−Y−Zr alloys [J]. Transactions of Nonferrous Metals Society of China, 2019, 29: 722−734.

[4] HOU Cai-hong, YE Zhi-song, QI Fu-gang, WANG Qing, LI Lian-hui, OUYANG Xiao-ping, ZHAO Nie. Effect of Al addition on microstructure and mechanical properties of Mg−Zn−Sn−Mn alloy [J]. Transactions of Nonferrous Metals Society of China, 2021, 31: 1951−1968.

[5] TANE M, NAGAI Y, KIMIZUKA H, HAGIHARA K, KAWAMURA Y. Elastic properties of an Mg−Zn−Y alloy single crystal with a long-period stacking-ordered structure [J]. Acta Materialia, 2013, 61: 6338−6351.

[6] HAGIHARA K, KINOSHITA A, SUGINO Y, YAMASAKI M, KAWAMURA Y, YASUDA H Y, UMAKOSHI Y. Effect of long-period stacking ordered phase on mechanical properties of $Mg_{97}Zn_1Y_2$ extruded alloy [J]. Acta Materialia, 2010, 58: 6282−6293.

[7] HAGIHARA K, KINOSHITA A, SUGINO Y, YAMASAKI M, KAWAMURA Y, YASUDA H Y, UMAKOSHI Y. Plastic deformation behavior of $Mg_{97}Zn_1Y_2$ extruded alloys [J]. Transactions of Nonferrous Metals Society of China, 2010, 20: 1259−1268.

[8] KAWAMURA Y, HAYASHI K, INOUE A, MASUMOTO T. Rapidly solidified powder metallurgy $Mg_{97}Zn_1Y_2$ alloys with excellent tensile yield strength above 600 MPa [J]. Materials Transactions, 2001, 42: 1172−1176.

[9] XU Chao, ZHENG Ming-yi, XU Shi-wei, WU Kun, WANG Er-de, KAMADO S, WANG Guo-jun, LV Xin-yu. Ultra high-strength Mg−Gd−Y−Zn−Zr alloy sheets processed by large-strain hot rolling and ageing [J]. Materials Science and Engineering A, 2012, 547: 93−98.

[10] MATSUDA M, II S, KAWAMURA Y, IKUHARA Y, NISHIDA M. Interaction between long period stacking order phase and deformation twin in rapidly solidified $Mg_{97}Zn_1Y_2$ alloy [J]. Materials Science and Engineering A, 2004, 386: 447−452.

[11] MATSUDA M, ANDO S, NISHIDA M. Dislocation structure in rapidly solidified $Mg_{97}Zn_1Y_2$ alloy with long period stacking order phase [J]. Materials Transactions, 2005, 46: 361−364.

[12] SHAO Xiao-hong, YANG Zhi-qing, MA Xiu-liang. Interplay between deformation twins and basal stacking faults enriched with Zn/Y in $Mg_{97}Zn_1Y_2$ alloy [J]. Philosophical Magazine Letters, 2014, 94: 150−156.

[13] PARTRIDGE P G. The crystallography and deformation modes of hexagonal close-packed metals [J]. International Materials Reviews, 1967, 12: 169−194.

[14] KOIKE J, OHYAMA R. Geometrical criterion for the activation of prismatic slip in AZ61 Mg alloy sheets deformed at room temperature [J]. Acta Materialia, 2005, 53: 1963−1972.

[15] OBARA T, YOSHINGA H, MOROZUMI S. $\{11\overline{2}\overline{2}\}\langle\overline{1}\overline{1}23\rangle$ slip system in magnesium [J]. Acta Metallurgica, 1973, 21: 845−853.

[16] REED-HILL R E, ROBERTSON W D. The crystallographic characteristics of fracture in magnesium single crystals [J]. Acta Metallurgica, 1957, 5: 728−737.

[17] HAGIHARA K, SUGINO Y, FUKUSUMI Y, UMAKOSHI Y, NAKANO T. Plastic deformation behavior of Mg12ZnY LPSO-Phase with 14H-typed structure [J]. Materials Transactions, 2011, 52: 1096−1103.

[18] LUO Xiao-mei, BI Guang-li, JIANG Jing, LI Ming, LI Rong-guang, LI Yuan-dong, MA Ying, HAO Yuan. Compressive anisotropy of extruded Mg−Dy−Zn alloy sheet [J]. Transactions of Nonferrous Metals Society of China, 2016, 26: 390−397.

[19] SHI Guo-liang, ZHANG Kui, LI Xing-gang, LI Yong-jun, MA Ming-long, YUAN Jia-wei, LU Chun-fang. Mixed grain structure and mechanical property anisotropy of AZ40 magnesium alloy bar with diameter of 160 mm [J]. Transactions of Nonferrous Metals Society of China, 2015, 25: 3944−3952.

[20] SHI Bin-qing, CHEN Rong-shi, KE Wei. Effects of processing route on texture and mechanical properties of WZ62 alloy [J]. Transactions of Nonferrous Metals Society of China, 2011, 21: 830−835.

[21] YI S B, DAVIES C H J, BROKMEIER H G, BOLMARO R E, KAINER K U, HOMEYER J. Deformation and texture evolution in AZ31 magnesium alloy during uniaxial loading [J]. Acta Materialia, 2006, 54: 549−562.

[22] HU Li, LV Hu-yuan, SHI Lai-xin, CHEN Yu, CHEN Qiang, ZHOU Tao, LI Ming-ao, YANG Ming-bo. Research on deformation mechanism of AZ31 magnesium alloy sheet with non-basal texture during uniaxial tension at room temperature: A visco-plastic self-consistent analysis [J]. Journal of Magnesium and Alloys, 2022, 10: 1994−2008.

[23] CHEN Tao, CHEN Zhi-yong, SHAO Jian-bo, WANG Ren-ke, MAO Long-hui, LIU Chu-ming. Evolution of LPSO phases in a Mg−Zn−Y−Gd−Zr alloy during semi-continuous casting, homogenization and hot extrusion [J]. Materials & Design, 2018, 152: 1−9.

[24] ALIZADEH R, MAHMUDI R, NGAN A H W, LANGDON T G. An unusual extrusion texture in Mg−Gd−Y−Zr alloys [J]. Advanced Engineering Materials, 2016, 18: 1044−1049.

[25] ZHANG Yu, RONG Wei, WU Yu-juan, PENG Li-ming. Achieving ultra-high strength in Mg−Gd−Ag−Zr wrought alloy via bimodal-grained structure and enhanced precipitation [J]. Journal of Materials Science & Technology, 2020, 54: 160−170.

[26] WU Shou-zhong, NAKATA T, TANG Guang-ze, XU Chao, WANG Xiao-jun, LI Xue-wen, QIAO Xiao-guang, ZHENG Ming-yi , GENG Lin, KAMADO S, FAN Guo-hua. Effect of forced-air cooling on the microstructure and age-hardening response of extruded Mg−Gd−Y−Zn−Zr alloy full with LPSO lamella [J]. Journal of Materials Science & Technology, 2021, 73: 66−75.

[27] IMANDOUST A, BARRETT C D, OPPEDAL A L, WHITTINGTON W R, PAUDEL Y, EL KADIRI H. Nucleation and preferential growth mechanism of recrystallization texture in high purity binary magnesium-rare earth alloys [J]. Acta Materialia, 2017, 138: 27−41.

[28] ZHANG Qian, LI Quan-an, CHEN Xiao-ya, ZHAO Jia-xin, BAO Jian, CHEN Zi-yi. Dynamic precipitation and recrystallization mechanism during hot compression of Mg−Gd−Y−Zr alloy [J]. Journal of Materials Research and Technology, 2021, 15: 37−51.

[29] LU Jia-wei, YIN Dong-di, HUANG Guang-hao, QUAN Gao-feng, ZENG Ying, ZHOU Hao, WANG Qu-dong. Plastic anisotropy and deformation behavior of extruded Mg−Y sheets at elevated temperatures [J]. Materials Science and Engineering A, 2017, 700: 598−608.

[30] SHAO Jian-bo, CHEN Zhi-yong, CHEN Tao, WANG Ren-ke, LIU Yao-ling, LIU Chu-ming. Texture evolution, deformation mechanism and mechanical properties of the hot rolled Mg−Gd−Y−Zn−Zr alloy containing LPSO phase [J]. Materials Science and Engineering A, 2018, 731: 479−486.

[31] HAGIHARA K, OKAMOTO T, YAMASAKI M, KAWAMURA Y, NAKANO T. Electron backscatter diffraction pattern analysis of the deformation band formed in the Mg-based long-period stacking ordered phase [J]. Scripta Materialia, 2016, 117: 32−36.

[32] HAGIHARA K, YOKOTANI N, UMAKOSHI Y. Plastic deformation behavior of Mg12YZn with 18R long-period stacking ordered structure [J]. Intermetallics, 2010, 18: 267−276.

[33] SHAO Jian-bo, CHEN Zhi-yong, CHEN Tao, LIU Chu-ming. The interaction between $\{10\overline{1}2\}$ twinning and long-period stacking ordered (LPSO) phase during hot rolling and annealing process of a Mg−Gd−Y−Zn−Zr alloy [J]. Metallurgical and Materials Transactions A, 2021, 52: 520−530.

[34] ROBSON J D, STANFORD N, BARNETT M R. Effect of precipitate shape on slip and twinning in magnesium alloys [J]. Acta Materialia, 2011, 59: 1945−1956.

[35] JIN Xue-ze, XU Wen-chen, YANG Zhong-ze, YUAN Can, SHAN De-bin, TENG Bu-gang, JIN Bo-cheng. Analysis of abnormal texture formation and strengthening mechanism in an extruded Mg−Gd−Y−Zn−Zr alloy [J]. Journal of Materials Science & Technology, 2020, 45: 133−145.

[36] KWAK T Y, KIM W J. Mechanical properties and Hall−Petch relationship of the extruded Mg−Zn−Y alloys with different volume fractions of icosahedral phase [J]. Journal of Alloys and Compounds, 2019, 770: 589−599.

[37] GAO Lei, CHEN Rong-shi, HAN En-hou. Effects of rare-earth elements Gd and Y on the solid solution strengthening of Mg alloys [J]. Journal of Alloys and Compounds, 2009, 481: 379−384.

[38] HE Shang-ming, ZENG Xiao-qin, PENG Li-ming, GAO Xiang, NIE Jian-feng, DING Wen-jiang. Microstructure and strengthening mechanism of high strength Mg−10Gd−2Y−0.5Zr alloy [J]. Journal of Alloys and Compounds, 2007, 427: 316−323.

[39] TAHREEN N, ZHANG Ding-fei, PAN Fu-sheng, JIANG Xian-quan, LI Dong-yang, CHEN Dao-lun. Strengthening mechanisms in magnesium alloys containing ternary I, W and LPSO phases [J]. Journal of Materials Science & Technology, 2018, 34: 1110−1118.

[40] WANG Ming, XU Xin-yu, WANG Hui-yuan, HE Lun-hua, HUANG Ming-xin. Evolution of dislocation and twin densities in a Mg alloy at quasi-static and high strain rates [J]. Acta Materialia, 2020, 201: 102−113.

[41] LI Xiao-qiang, REN Liang, LE Qi-chi, BAO Lei, JIN Pei-peng, WANG Ping, CHENG Chun-long, ZHOU Xiong, HU Cheng-lu. Reducing the yield asymmetry in Mg−5Li−3Al−2Zn alloy by hot-extrusion and multi-pass rolling [J]. Journal of Magnesium and Alloys, 2020, 9: 937−949.

[42] HANSEN N, HUANG Xiao-xu. Microstructure and flow stress of polycrystals and single crystals [J]. Acta Materialia, 1998, 46: 1827−1836.

含不同初始织构的 Mg−Gd−Y−Zn−Zr 合金热轧板材的显微组织和力学性能

陈 汉，胡 璋，韩宇翔，陈 韬，刘楚明，陈志永

中南大学 材料科学与工程学院，长沙 410083

摘 要：通过光学显微镜、扫描电子显微镜、电子背散射衍射、透射电子显微镜和拉伸试验研究含不同初始织构的 Mg−4.7Gd−3.4Y−1.2Zn−0.5Zr (质量分数，%) 合金热轧板材的显微组织和力学性能。结果表明，初始织构为⟨0001⟩//RD(板材轧向)的板材获得相对较粗的晶粒和双峰基面织构；而初始织构为⟨0001⟩//TD(板材横向)的板材动态再结晶程度更高，因此，获得更细的晶粒尺寸和较强的⟨0001⟩//ND 基面织构。此外，在两种板材中均发现沿 RD 拉长的不规则形状 LPSO 相，这种 LPSO 相导致各向异性的承载强化行为，并进一步引起板材的屈服各向异性。对强化机理的分析表明，晶界强化对轧制板材的强化效果最好。由于具有较小的晶粒尺寸和 LPSO 相带来的承载强化效果，初始织构为⟨0001⟩//TD 的板材在 RD 方向上获得最高的屈服强度。

关键词：Mg−Gd−Y−Zn−Zr 合金；织构；LPSO 相；力学性能；强化机理

(Edited by Xiang-qun LI)